Research on Iron Loss of Switched Reluctance Starter/Generator for Energy Storage

Hao Chen, Xing Wang, Yongqiang Liu, Vuong Dang Quoc, Wenju Yan, Muhammad Saqib, Antonino Musolino, Guanjun Wang, Yong Qi, Ali Asghar Memon, and Alexandros G. Paspatis

***Abstract*—In order to better realize the energy recovery and storage of hybrid EVs (HEVs), a switched reluctance starter/generator (SRS/G) with both starting and power generation functions is investigated in this paper. First, the iron loss of SRS/G is mainly studied to reduce the motor loss and improve the power generation efficiency. Then, the energy storage of hybrid EVs can be effectively improved. Secondly, a magnetic flux density (MFD) waveforms solution method is proposed to solve the difficulty in calculating the iron loss of the SRS/G. Compared with the commonly used finite element method, the proposed solution method has the advantages of simple, fast and small computational amount. Meanwhile, considering the different operating conditions of SRS/G, the iron loss models for both the time-domain and frequency-domain are established. In addition, the calculation formula of the variable coefficient Bertotti three-term loss separation is improved. As the hysteresis loss coefficient, the Steinmetz coefficient and the stray loss coefficient are respectively fitted by the Fourier fitting method. This method is also applied to solve the iron loss of SRS/G. Finally, through an experimental verification, it is indicated that the development of proposed method has high accuracy.**

***Index Terms*—Switched reluctance starter/generator, energy storage, iron loss, finite element method, magnetic flux density (MFD).**

I. INTRODUCTION

Low-carbon emission reduction and clean energy power generation are related to the future survival and development of mankind, and have become the consensus and struggling goal of most countries around the world [1], [2]. Due to the promotion of low-carbon energy, new energy vehicles have become the first choice for people's travel. Meanwhile, the new energy vehicles have also become the focus of industrial development and policy support. Many scholars are committed to researching clean fuels and energy recovery devices to help cars save energy and reduce carbon emissions. Based on the analysis of performance indicators such as system efficiency, fuel tank compactness and the driving range, ammonia can be used as a sustainable fuel for power generation on vehicles [3]. Hydrogen produced from renewable energy can be used as fuel for fuel cell electrical vehicles (EVs), and a cost model is established to assess the cost and competitiveness of driving fuel cell EVs, fueled by the hydrogen produced from renewables [4]. In terms of energy recovery device research, heavy-duty vehicles can realize energy reuse/recovery by adopting a novel design of a compound coupled hydro-mechanical transmission [5].

Received: August 1, 2023
Accepted: March 19, 2024

Hao Chen (corresponding author) is with the Shenzhen Research Institute, China University of Mining and Technology, Shenzhen 515100, China; the School of Electrical Engineering, China University of Mining and Technology, Xuzhou 221116, China; Xinjiang Institute of Engineering, Urumqi 830000, China; the International Joint Research Center of Central and Eastern European Countries on New Energy EV Technology and Equipment, Xuzhou 221008, China; the International Cooperation Joint Laboratory of New Energy Power Generation and EVs of Jiangsu Province Colleges and Universities, Xuzhou 221008, China; and also with the Xuzhou Key Laboratory of New Energy EV Technology and Equipment, Xuzhou 221008, China (e-mail: hchen@cumt.edu.cn).

Xing Wang is with the Shenzhen Research Institute, China University of Mining and Technology, Shenzhen 515100, China; the International Joint Research Center of Central and Eastern European Countries on New Energy EV Technology and Equipment, Xuzhou 221008, China (3512@cumt.edu.cn).

DOI: 10.23919/PCMP.2023.000031

Yongqiang Liu and Wenju Yan are with the the School of Electrical Engineering, China University of Mining and Technology, Xuzhou 221116, China (860936052@qq.com; yanwenju09@126.com).

Vuong Dang Quoc is with the Laboratory of High Performance Electric Machines (HiPems), Hanoi VN 10000, Viet Nam (vuong.dangquoc@hust.edu.vn).

Muhammad Asghar Saqib is with the University of Engineering and Technology, Lahore 54890, Pakistan (asgharsaqib@gmail.com).

Antonino Musolino is with the Department of Energy Pisa, University of Pisa, Pisa IT 56126, Italy (antonino. musolino@unipi.it).

Guanjun Wang is with the Wuxi Inspection and Testing Certification Research Institute, Wuxi 214000, China (wgjcumt@126.com).

Yong Qi is with the Nanjing University of Science & Technology, Nanjing 210094, China (790815561@qq.com)

Ali Asghar Memon is with the Mehran University of Engineering & Technology, Jamshoro PK 76062, Sindh (ali.asghar@faculty.muet.edu.pk).

Alexandros G. Paspatis is with the National Technical University of Athens, Zografou GR 15780, Attica (agpaspatis@mail.ntua.gr).

Moreover, the energy recovery of hybrid vehicles can be achieved through the development and equipment of starters/generators.

Integrated starter/generator (ISG) technology integrates the functions of traditional starter and generator units, and is widely used in power systems of hybrid EVs and aviation equipment [6]–[8]. The starter/generator system is mainly composed of starter/generator, power converter, controller and high power density battery pack. Only one motor is adopted to achieve two states of electric and power generation in the starter/generator system. The weight, cost, and space occupation of the hybrid EV power system can be effectively reduced. The starter/generator system can realize energy recovery and energy storage for hybrid EVs, which makes the system more efficient, saves fuel, and achieves low emissions and low noise. Hybrid EV equipped with a starter/generator system are one of the practical products for the transition from conventional engine vehicles to zero-emission EVs [9]–[11]. The rotating motors used in starter/generator systems mainly include permanent magnet motor, switched reluctance motor (SRM) and induction motor. With the advantages of low cost, high reliability, high power density and adaptability to high speed and high temperature operation, the SRM has become one of the best choices for the starter/generator of a hybrid EV [12]–[14].

Iron loss is a major factor to improve the operating efficiency of a switched reluctance starter/generator (SRS/G), so how to reduce the iron loss of SRS/G has become a research hotspot. Due to its doubly salient structure, the power supply waveform of SRM is more complicated than that of other commonly used motors, and the local magnetic flux saturation phenomenon will occur. Moreover, the nonlinear and non-sinusoidal characteristics of the magnetic flux waveform of each part of the machine make the calculation of core loss particularly complicated [15]. The solutions of magnetic flux density waveforms of motors are mainly divided into traditional iron loss calculation method [16], equivalent magnetic circuit method [17]–[19] and finite element method [20], [21]. In recent years, a model for quickly solving the magnetic flux density waveforms has not only increased the accuracy and rapidity of the solution, but also greatly improved the universality of the solution [22].

Both the stator and rotor of SRM are made of ferromagnetic silicon steel sheets, then the iron loss model of SRM is mostly based on the improvement of the iron loss solution model of ferromagnetic materials. In [23], a variable coefficient iron loss model adopted the rainflow counting method is established to solve the local hysteresis loop problem of hysteresis loss, and the influence of various control parameters on the SRM iron loss under PWM control is analyzed. It is found that the iron loss can be reduced when the SRM operates under PWM control mode, using a smaller duty cycle and smaller conduction angle [24]. In [25], a new type of SRM structure is designed for the starting generator of aircraft. At the same time, finite element analysis software is used to obtain the magnetic density waveform of the new motor, and the iron core loss of the motor is calculated using the Bertotti iron loss model. The results show that the loss of the motor is relatively low compared to a conventional SRM.

In recent years, the research on iron loss of SRM are mainly based on the electric state [26], [27], and there are few literature studies the iron loss of SRM when it is used as starter and generator. As the SRS/G is more and more widely used, the study of its iron loss is of great help to improve efficiency and optimize motor design. Meanwhile, the traditional method for solving magnetic flux density waveforms is to perform finite element simulation on the SRM of a certain working condition to obtain the transient magnetic flux density waveform of the representative part. If the working condition changes, it is necessary to perform finite element simulation again, and the calculation process is relatively complex. To solve the above questions, the magnetic circuit direction of SRM is analyzed to obtain the corresponding magnetic circuit formula, a combination of finite element and magnetic circuit methods is adopted to calculate the iron loss of the motor, effectively reducing the calculation time of iron loss. At the same time, the existing magnetic density waveform fitting method is improved. Then the calculation accuracy of iron loss of the motor in electric and power generation states is also improved.

This paper is organized as follows. The solution of magnetic flux density waveforms is described in Section II. The improved iron loss models are established in Section III. In Section IV, the results of iron loss at different stages of SRS/G are solved. The validation experiments and comparative analysis are conducted in Section V. Conclusions are shown in Section VI.

II. SOLUTION OF MAGNETIC MAGNETIC FLUX DENSITY WAVEFORMS

A. Solution of Transient Magnetic Flux Density of Stator Poles

Taking the stator pole A as an example, the transient magnetic flux density of a certain part of the SRS/G includes not only the magnetic flux density generated by the main magnetic flux when phase A is turned on, but also the magnetic flux density generated by the leakage magnetic flux when phase B and phase C are turned on. Therefore, the solution of static magnetic flux density needs to establish static models for analysis when phase A, phase B, and phase C are excited separately.

The geometric parameters of the SRS/G prototype are shown in Table I, and the electromagnetic simulation model is established in the finite element software FLUX according to these geometric parameters data. The sensors are established on the stator pole A, stator pole B and stator pole C to obtain the static magnetic flux density waveforms, and the location distribution of these sensors are shown in Fig. 1. It can be seen that when only phase A is turned on, the main magnetic flux mainly passes through the stator pole A, the magnetic flux density is large. The leakage magnetic flux mainly passes through the stator pole B and stator pole C, and the magnetic flux density is small.

Then the magnetic flux density can be obtained by the sensors. According to the static finite element model of SRS/G, the relationships between the radial and tangential static magnetic flux density of the central position of the stator pole A, the currents and the rotor positions are obtained when phase A, phase B, and phase C are separately turned on. Therefore, the radial and tangential components of the static magnetic flux density waveforms in the middle position of the stator pole A can be obtained.

After the radial static magnetic density components $B_{\mathrm{spA\,AR}}$, $B_{\mathrm{spA\,BR}}$ and $B_{\mathrm{spA\,CR}}$ of stator pole A (spA) are obtained when phase A, B, and C are respectively turned on, these data are imported into to a two-dimensional look-up table established in MATLAB/Simulink. According to the three-phase currents i_{a}, i_{b} and i_{c} and rotor positions θ_{a}, θ_{b} and θ_{c} calculated in the established nonlinear SRS/G model [19], the radial transient magnetic flux density of spA is obtained, and the solving module for calculating $B_{\mathrm{spA\_R}}$ is shown in Fig. 2. It only needs to replace the radial static magnetic flux density components shown in Fig. 2 with the tangential static magnetic flux density components $B_{\mathrm{spA\,AT}}$, $B_{\mathrm{spA\,BT}}$ and $B_{\mathrm{spA\,CT}}$ to solve the tangential transient magnetic flux density $B_{\mathrm{spA\,T}}$. The transient magnetic flux density of the stator pole B (spB) and stator pole C (spC) can be obtained with the same solving process.

TABLE I

PROTOTYPE GEOMETRIC PARAMETERS

Parameters	Symbols	Values
Stator outer diameter	D_{s}	122.5 mm
Stator yoke thickness	h_{sy}	11.00 mm
Stator pole arc angle	β_{s}	32.88°
Air gap	δ	0.30 mm
Rotor outer diameter	D_{r}	62.5 mm
Rotor yoke thickness	h_{ry}	11.00 mm
Rotor pole arc angle	β_{r}	34.69°
Shaft diameter	D_{sh}	20.00 mm
Lamination thickness	L_{stk}	70.00 mm
Turns per phase winding	N	72

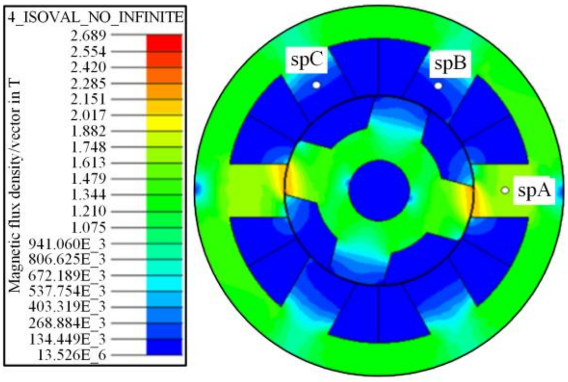

Fig. 1. The positions of the sensors spA, spB and spC when phase A is energized individually.

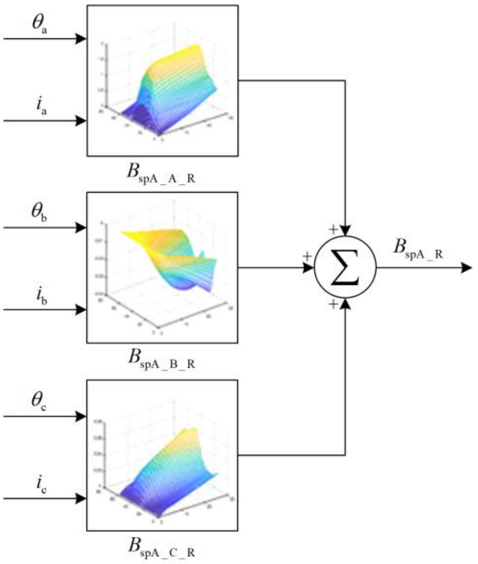

Fig. 2. Transient radial flux waveform solving module of spA.

B. *Solution of Transient Magnetic Flux Density of the Rest of the Machine*

1) Relationship Between the Transient MFD of the Rest Part and the Transient MFD of Stator Pole

The prototype selected in this paper is a three-phase 6/4 structure SRS/G with NNNSSS polarity distribution. The transient magnetic flux linkage of each phase is basically the same, but there is one or two power cycle TD phase difference. Therefore, the magnetic flux linkage of the other two phases can be deduced if magnetic flux linkage of phase A is known. The windings of each phase are wrapped around the stator pole, so the transient magnetic flux linkage of each phase is almost the same as the magnetic flux waveform of the stator pole. Then the magnetic flux waveforms of stator yoke, rotor pole and rotor yoke can be obtained according to the magnetic flux path of the SRS/G, which is called the magnetic circuit analytic method. The magnetic flux path direction and polarity distribution of SRS/G are shown in Fig. 3.

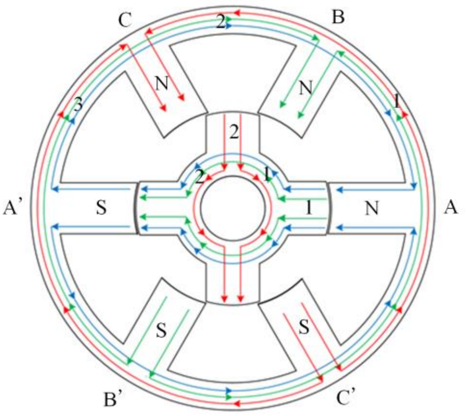

Fig. 3. Magnetic flux path of SRS/G with NNNSSS polarity distribution.

Based on the operation principle of SRM, when the rotor of the SRS/G rotates in a counterclockwise direction(A-B-C-A'-B'-C'), the excitation sequence of three-phase windings is A-C'-B'-A'-C-B. In this paper, the positive direction of yoke magnetic flux is defined as clockwise direction, and the positive direction of pole magnetic flux is defined as the direction from outer diameter to inner diameter.

The magnetic flux waveforms of spA, spB and spC are respectively expressed as $\phi_{\mathrm{spA}}(t)$, $\phi_{\mathrm{spB}}(t)$ and $\phi_{\mathrm{spC}}(t)$. Then the expressions of magnetic flux waveforms of stator yoke are shown as:

$$\begin{cases} \phi_{\mathrm{sy1}}(t)=(\phi_{\mathrm{spA}}(t)-\phi_{\mathrm{spB}}(t)-\phi_{\mathrm{spC}}(t))/2 \\ \phi_{\mathrm{sy2}}(t)=(\phi_{\mathrm{spA}}(t)+\phi_{\mathrm{spB}}(t)-\phi_{\mathrm{spC}}(t))/2 \\ \phi_{\mathrm{sy3}}(t)=(\phi_{\mathrm{spA}}(t)+\phi_{\mathrm{spB}}(t)+\phi_{\mathrm{spC}}(t))/2 \end{cases} \tag{1}$$

The expressions of magnetic flux waveforms of the rotor poles and the rotor yoke are expressed as:

$$\phi_{\mathrm{rp1}}(t)=\begin{cases} \phi_{\mathrm{spA}}(t), & 0°\leqslant\theta<60° \\ \phi_{\mathrm{spB}}(t), & 60°\leqslant\theta<120° \\ \phi_{\mathrm{spC}}(t), & 120°\leqslant\theta<180° \\ -\phi_{\mathrm{spA}}(t), & 180°\leqslant\theta<240° \\ -\phi_{\mathrm{spB}}(t), & 240°\leqslant\theta<300° \\ -\phi_{\mathrm{spC}}(t), & 300°\leqslant\theta<360° \end{cases} \tag{2}$$

$$\phi_{\mathrm{rp2}}(t)=\phi_{\mathrm{rp2}}(t-T_{\mathrm{s}}) \tag{3}$$

$$\phi_{\mathrm{ry1}}(t)=(\phi_{\mathrm{rp2}}(t)-\phi_{\mathrm{rp1}}(t))/2 \tag{4}$$

$$\phi_{\mathrm{ry2}}(t)=-(\phi_{\mathrm{rp2}}(t)+\phi_{\mathrm{rp1}}(t))/2 \tag{5}$$

The changing frequency of the stator magnetic flux density waveforms depends on the switching frequency of the windings. When the three-phase windings of the 6/4 structure SRS/G are energized once, the rotor rotates through 90°, and the stator magnetic flux density waveform also passes through a period T_{s}. Thus, the expression of changing period T_{s} of stator magnetic flux density waveform is shown as:

$$T_{\mathrm{s}}=\frac{60}{nN_{\mathrm{r}}}=\frac{2\pi}{\omega N_{\mathrm{r}}} \tag{6}$$

where n is rotational speed; N_{r} is rotor pole number; and ω is angular velocity.

The expression of power cycle is shown as:

$$T_{\mathrm{D}}=\frac{60}{qnN_{\mathrm{r}}}=\frac{2\pi}{q\omega N_{\mathrm{r}}} \tag{7}$$

where q is the number of phases.

The magnetic flux density waveform B_{xxx} can be obtained by dividing the solution result of the magnetic flux waveform ϕ_{xxx} by the product of the area S_{xxx} of the magnetic flux path and the number of winding turns N .

$$B_{xxx}=\frac{\phi_{xxx}}{NS_{xxx}} \tag{8}$$

where suffix xxx represents each part of the SRS/G, such as spA, spB and spC of the stator poles; sy1, sy2 and sy3 of the stator yoke; rp1 and rp2 of the rotor poles and ry1 and ry2of the rotor yoke.

2) Transient Magnetic Flux Density of Each Part

The radial and tangential magnetic flux density waveforms of stator pole spA, spB and spC are obtained by finite element method (FEM).

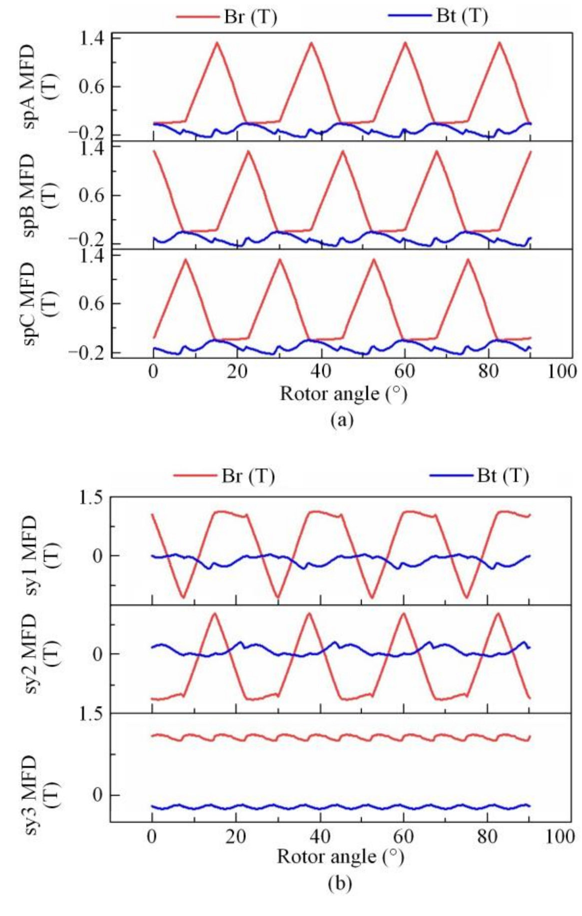

(a)

(b)

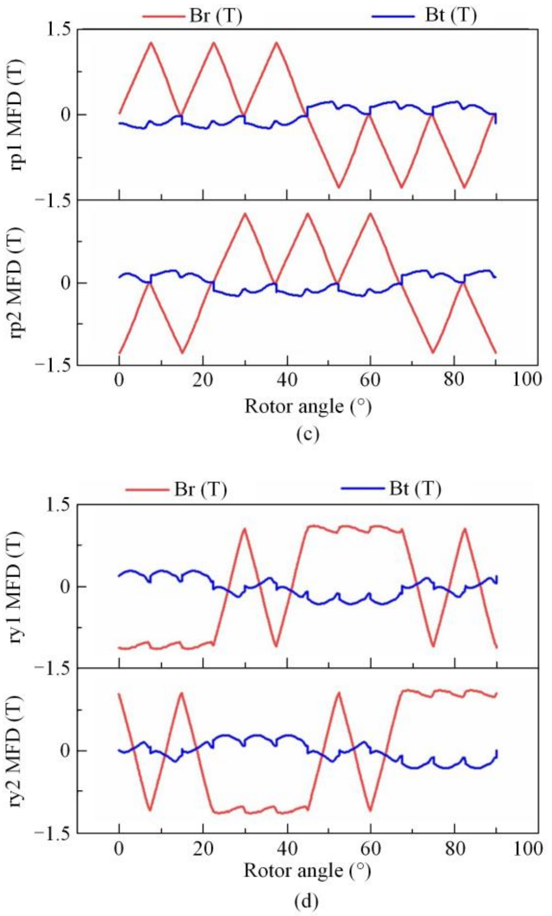

(c)

(d)

Fig. 4. Magnetic density waveform of each part of the motor with NNNSSS polarity distribution. (a) The radial and tangential magnetic flux density waveforms of stator pole spA, spB and spC. (b) The radial and tangential magnetic flux density waveforms of stator yoke sy1, sy2 and sy3. (c) The radial and tangential magnetic flux density waveforms of rotor pole rp1 and rp2. (d) The radial and tangential magnetic flux density waveforms of rotor yoke ry1 and ry2.

The radial and tangential magnetic flux density waveforms of stator yoke sy1, sy2 and sy3, rotor pole rp1 and rp2 and rotor yoke ry1 and ry2 can be obtained according to the relationship of magnetic flux waveforms between the stator poles part and other parts. The magnetic flux waveforms of each part of the machine obtained by this method are shown in Fig. 4.

III. IRON LOSS MODEL

A. Fitting of Iron Loss Model Coefficients

In the previous section, the obtained magnetic flux density waveform of SRS/G is non-sinusoidal, and the operating frequency range of SRS/G is relatively wide. Then, the Jordan and Bertotti models with constant coefficients will no longer be applicable. When the magnetic flux density waveform is an arbitrary waveform, a calculation method is proposed in [15] to solve the iron loss, which is expressed as:

$$P_{\text{iron}} = P_h + P_e + P_{ex} = k_h(B_m)B_m^{\alpha(B_m)}\frac{1}{T} + \frac{k_e(B)}{2\pi^2}\frac{1}{T}\int_T\left(\frac{\mathrm{d}B}{\mathrm{d}t}\right)^2\mathrm{d}t + \frac{k_{ex}(B)}{8.763}\frac{1}{T}\int_T\left|\frac{\mathrm{d}B}{\mathrm{d}t}\right|^2\mathrm{d}t \tag{9}$$

This method is adopted to solve the iron loss in the time-domain. When the SRM is in the starting stage, the magnetic flux waveform is irregular, and the frequency increases with the continuous increase in the speed of SRS/G. Therefore, this method is suitable for solving the iron loss of switched reluctance starter (SRS).

However, the more accurate and commonly used method is to solve the iron loss in the frequency-domain. The frequency-domain iron loss model is suitable for solving the magnetic flux waveforms in the form of sine waves. If the magnetic flux density waveform is non-sinusoidal, it is necessary to expand the magnetic flux density waveform by Fourier series, so that the non-sinusoidal waveform is expanded into fundamental and multiple harmonics. The expression of iron loss model in frequency-domain is as follows:

$$P_{\text{iron}} = P_h + P_e + P_{ex} = k_h(B)B^{\alpha(B)}f + k_e B^2 f^2 + k_{ex}(B)B^{1.5}f^{1.5} \tag{10}$$

where $k_h(B)$, $\alpha(B)$, k_e and $k_{ex}(B)$ are the hysteresis loss coefficient, Steinmetz coefficient, eddy current loss coefficient and stray loss coefficient, respectively.

And the eddy current loss coefficient is expressed as:

$$k_e = \frac{\pi^2\sigma d^2}{6\rho} \tag{11}$$

where ρ is the density of the silicon steel sheet (kg/m^3); σ is the electrical conductivity of the silicon steel sheet (S/m); and d is the thickness of the silicon steel sheet (m).

Considering the large error of polynomial fitting method in the region with small magnetic flux density, the iron loss calculation formula is deformed in this paper, and each coefficient is improved by Fourier fitting method. The improved formula is as follows:

$$P_{\text{iron}} = af + k_e B^2 f^2 + k_{ex}(B)B^{1.5}f^{1.5} \tag{12}$$

The solving expressions of each coefficient in the above equation are as follows:

$$a = k_h(B)B^{\alpha(B)} \tag{13}$$

$$\begin{cases} k_h(B) = k_{h0} + k_{h1}\cos(\omega_h B) + k_{h2}\sin(\omega_h B) + \\ \qquad k_{h3}\cos(2\omega_h B) + k_{h4}\sin(2\omega_h B) \\ \alpha(B) = \alpha_0 + \alpha_1\cos(\omega_\alpha B) + \alpha_2\sin(\omega_\alpha B) \\ k_{ex}(B) = k_{ex0} + k_{ex1}\cos(\omega_{ex} B) + k_{ex2}\sin(\omega_{ex} B) + \\ \qquad k_{ex3}\cos(2\omega_{ex} B) + k_{ex4}\sin(2\omega_{ex} B) \end{cases} \tag{14}$$

According to the above expressions, the specific loss value of silicon steel sheet is used for regression analysis, and the calculation expressions of each coefficient are obtained as follows:

$$\begin{cases} k_h(B) = -0.1304 + 0.08031\cos(0.998B) + \\ \qquad 0.1944\sin(0.998B) + \\ \qquad 0.05498\cos(2\times 0.998B) - \\ \qquad 0.03261\sin(2\times 0.998B) \\ \alpha(B) = 0.01812 + 1.476\cos(0.004729B) + \\ \qquad 93.37\sin(0.004729B) \\ k_{ex}(B) = 0.002537 - 0.002592\cos(1.848B) - \\ \qquad 0.0009005\sin(1.848B) + \\ \qquad 0.0003287\cos(2\times 1.848B) + \\ \qquad 0.0004289\sin(2\times 1.848B) \end{cases} \tag{15}$$

The fitting results of the coefficients a and k_{ex} are shown in Fig. 5. The comparison and error analysis between the specific loss obtained by this fitting method and the specific loss measured by the experiment are shown in Fig. 6 and Fig. 7, respectively. In Fig. 6, the curves with the suffix F represent the specific loss obtained by fitting, and the curves with the suffix E represent the specific loss obtained from the experiment. It can be seen that the specific loss curve obtained by the improved iron loss calculation model proposed in this paper is in good agreement with that of the experimental measurement, and the error between them is also small.

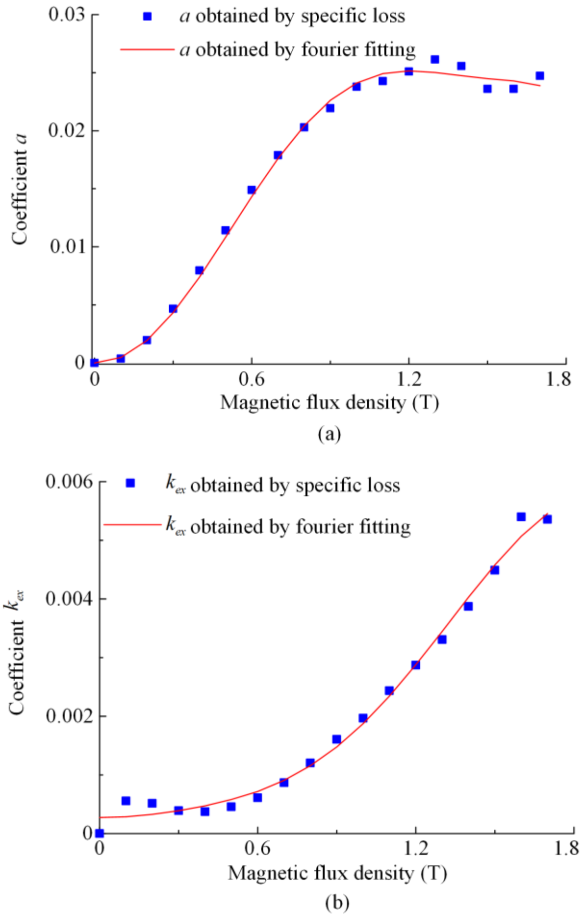

(a)

(b)

Fig. 5. Coefficient a and k_{ex} fitting comparison. (a) Coefficient a. (b) Coefficient k_{ex}.

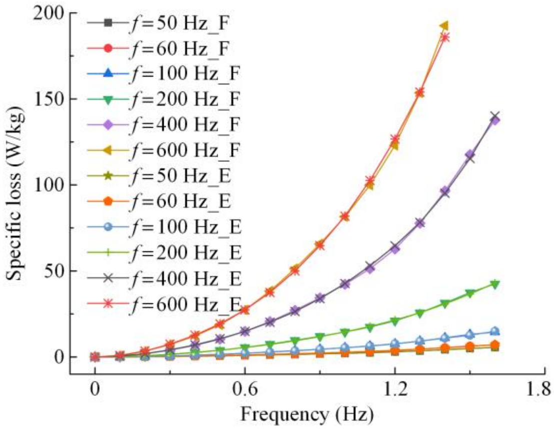

Fig. 6. Comparison of ratio loss at different frequencies ob-tained by fitting and experiment.

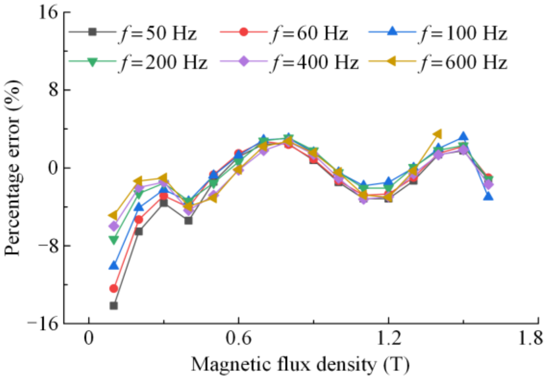

Fig. 7. Relative error at different frequencies obtained by fitting and experiment.

B. Improved Model Considering Small Hysteresis Loop and Skin Effect

It can be seen from Fig. 7 that the error of specific loss data obtained by the Fourier fitting variable coefficient iron loss model is large when the magnetic flux density value is small. In order to improve the accuracy of the model, the influence of small magnetic hysteresis loop on the calculation of hysteresis loss must be considered. The influence coefficient of small magnetic hysteresis loop is shown as:

$$K(B_m) = \frac{0.65}{B_m}\sum_{i=1}^{n}(B_{mi} - B_{li}) \tag{16}$$

where B_{mi} is the ith peak value of the small hysteresis loop; and B_{li} is the ith valley value of the small hysteresis loop.

When the changing frequency of magnetic flux density in silicon steel sheet is small, the skin effect is not obvious. Once the frequency increases, the skin effect will lead to the uneven distribution of eddy current in silicon steel sheet, which will affect the calculation of eddy current loss. Therefore, the eddy current loss coefficient needs to be multiplied by the skin effect coefficient to reduce the error. The expression of the skin effect coefficient is shown as:

$$k_{\mathrm{skin}}(f)=\frac{3}{D\sqrt{f}}\frac{\sin h(D\sqrt{f})-\sin(D\sqrt{f})}{\cos h(D\sqrt{f})-\cos(D\sqrt{f})} \tag{17}$$

The expression of coefficient is as follows:

$$D=d\sqrt{\pi\mu\sigma} \tag{18}$$

where μ is the average permeability of silicon steel; d is the thickness of the silicon steel sheet.

During the operation of SRS/G, it is not only affected by alternating magnetization, but also by rotation magnetization. Therefore, this paper divides the magnetic flux density waveform into radial component and tangential component to improve the accuracy of iron loss calculation. The iron loss models for both time and frequency domains are shown in (19) and (20), respectively.

$$\begin{cases} P_h=K(B_{rm})k_h(B_{rm})B_{rm}^{\alpha(B_{rm})}\dfrac{1}{T}+K(B_{tm})k_h(B_{tm})B_{tm}^{\alpha(B_{tm})}\dfrac{1}{T} \\ P_e=k_{\mathrm{skin}}(f)\dfrac{1}{T}\left[\dfrac{k_e(B_r)}{2\pi^2}\displaystyle\int_T\left(\dfrac{\mathrm{d}B_r}{\mathrm{d}t}\right)\mathrm{d}t+\dfrac{k_e(B_t)}{2\pi^2}\displaystyle\int_T\left(\dfrac{\mathrm{d}B_t}{\mathrm{d}t}\right)\mathrm{d}t\right] \\ P_{ex}=\dfrac{k_{ex}(B_r)}{8.763}\dfrac{1}{T}\displaystyle\int_T\left|\dfrac{\mathrm{d}B_r}{\mathrm{d}t}\right|^{1.5}\mathrm{d}t+\dfrac{k_{ex}(B_t)}{8.763}\dfrac{1}{T}\displaystyle\int_T\left|\dfrac{\mathrm{d}B_t}{\mathrm{d}t}\right|^{1.5}\mathrm{d}t \end{cases} \tag{19}$$

$$\begin{cases} P_h=K(B_{rm})k_h(B_{rm})B_{rm}^{\alpha(B)}f+K(B_{tm})k_h(B_{tm})B_{tm}^{\alpha(B)}f \\ P_e=\displaystyle\sum_{n=1}^{N}k_{\mathrm{skin}}(nf)k_e(B_{rn})B_{rn}^2(nf)^2+ \\ \qquad\displaystyle\sum_{n=1}^{N}k_{\mathrm{skin}}(nf)k_e(B_{tn})B_{tn}^2(nf)^2 \\ P_{ex}=\displaystyle\sum_{n=1}^{N}k_{ex}(B_{rn})B_{rn}^{1.5}(nf)^{1.5}+\sum_{n=1}^{N}k_{ex}(B_{tn})B_{tn}^{1.5}(nf)^{1.5} \end{cases} \tag{20}$$

IV. SOLUTION OF IRON LOSS OF SRS/G

A. Solution of Iron Loss in Starting Stage

The SRS/G is a SRM that integrates two different working states of starting and power generation. The motor first operates in the form of a starter, and its speed rises gradually from the stationary state. The starting stage is very short. When the starter drives the engine to the idling condition, the motor then operates in the form of generator driven by the engine. According to the changing frequency characteristics of the stator and rotor magnetic flux density of the SRS/G, the frequency of the machine is constantly changing under the starting state. Therefore, the frequency-domain iron loss model cannot be used to solve the iron loss generated during this stage, and the time-domain model must be used to solve it. The power generation state is the normal working state of SRS/G, and both iron loss solution models for the time and frequency domains are both applicable in this working state.

The iron loss of the motor is essentially a kind of power, which is a physical quantity to measure the energy consumption per unit time. The iron loss can be solved under the constant working condition of the motor, but it is no longer applicable to the starting stage of the SRS/G, because the speed and frequency constantly increases during the starting stage, which is not a constant working condition. In this paper, the integral of iron loss power with respect to time is calculated during the starting stage of SRS/G, and the energy W_{iron} consumed in the process from the stationary state to the idling speed is obtained. The specific solution expression is as follows:

$$W_{\mathrm{iron}}=\int_0^{t_0}P_{\mathrm{iron}}(t)\,\mathrm{d}t \tag{21}$$

where $P_{\mathrm{iron}}(t)$ is the iron loss power at a certain moment; and t_0 is the time required for SRS/G to reach idling speed from the stationary state.

TABLE II
ENERGY CONSUMED BY THE IRON LOSS OF NNNSSS POLAR DISTRIBUTION DURING THE STARTING PERIOD

Turn-on and turn-off angles (°)	Stator pole (J)	Stator yoke (J)	Rotor pole (J)	Rotor yoke (J)	Total energy (J)
0–30	45.22	92.48	19.98	21.96	179.64
−2–30	55.13	104.01	21.75	24.56	205.45
−2–32	57.71	122.72	22.01	26.43	228.87

TABLE III
ENERGY CONSUMED BY THE IRON LOSS OF NNNSSS POLAR DISTRIBUTION DURING THE STARTING PERIOD

Turn-on and turn-off angles (°)	Stator pole (J)	Stator yoke (J)	Rotor pole (J)	Rotor yoke (J)	Total energy (J)
0–30	44.48	91.71	5.67	7.16	149.02
−2–30	54.81	103.8	5.39	7.76	171.76
−2–32	57.39	122.6	5.17	8.35	193.51

In order to explore the influence of polarity distribution and turn-on and turn-off angles on the iron loss of SRS, the energy consumed by the iron loss of each part of SRS under different polarity distribution and different turn-on and turn-off angles is solved according to (18) and (20). The solution results are shown in Table II and Table III.

By comparing the data in the above two tables, it is found that the energy loss of NNNSSS polarity distribution is smaller, because the frequency of the rotor magnetic flux density waveform under the NSNSNS polarity distribution is three times that under the NNNSSS polarity distribution. With the increase of the conduction angle, regardless of the polarity distribution is NSNSNS or NNNSSS, the energy consumed by the iron loss is increased. No matter the turn-on angle moves forward, the turn-off angle moves backward, or both occur at simultaneously, the peak value of the current will increase, so that the magnetic flux density induced by the winding current will increase, and finally the iron loss will increase.

B. Solution of Iron Loss in Power Generation Stage

Compared with the starting stage, the iron loss calculation in the power generation stage is conventional, and the iron loss under specific condition such as a certain speed and a certain turn-on and turn-off angle can be calculated. When the rotational speed is constant, the changing frequencies of magnetic flux density waveform of the stator and rotor are also constant. Although the magnetic flux density waveform is not sinusoidal, the magnetic flux density waveforms of the stator and rotor can be decomposed by Fourier series, and the expression form of the sum of the fundamental and each harmonic can be obtained, which solves the problem that the frequency-domain model is only applicable to calculate the sinusoidal magnetic flux density waveforms. Therefore, the iron loss calculation of SRG can not only use the time-domain solution model, but also use the frequency-domain solution model.

The changing frequency of rotor magnetic flux density waveform is different from that of stator magnetic flux density waveform. It is related to the number of periods of winding polarity distribution. In this paper, the polarity distribution of SRG with three-phase 6/4 structure is NNNSSS, and then the number of periods of its polarity distribution is $K=1$. Then the expression of the changing frequency of the rotor magnetic flux density waveform is shown as:

$$f_{\mathrm{r}}=\frac{1}{T_{\mathrm{r}}}=\frac{nK}{60}=\frac{\omega K}{2\pi} \tag{22}$$

where T_{r} is the changing period of the rotor magnetic flux density; and K is the number of periods of winding polarity distribution.

Due to the existence of small hysteresis loop, the accuracy of hysteresis loss calculated by Fourier series expansion is not high, so the hysteresis loss cannot be solved directly by Fourier series expansion. According to (19), the hysteresis loss is not expanded by Fourier series, and the eddy current loss and stray loss are solved by Fourier series expansion.

In order to explore the influence of speed, turn-on angle and turn-off angle on the iron loss of SRG, the polarity distribution of SRG is set to NNNSSS in this paper, and the magnetic flux density waveform is solved by the method which combines the finite element method and the magnetic circuit analysis method. The obtained iron loss of each part of the machine under various working conditions is shown from Table IV to Table VI. In accordance with the above simulation data, it can be found that the iron loss increases with the increase of the conduction angle. This is because the peak value of the current in the winding increases with the increase of the conduction angle, and the magnetic flux density induced in the silicon steel sheet increases accordingly, so that the iron loss will increase. And the iron loss gradually increases with the increase of rotational speed. This is because the changing frequency of the magnetic flux density waveform increases with the increase of the rotational speed. The proportions of iron loss generated by various parts of the SRS/G are different, and the ratio of iron loss produced by the stator part and the rotor part is about 4:1. Firstly, the stator and the rotor are different from each other in weight, and the mass of the stator and the rotor is 3.15 kg and 0.99 kg, respectively.

TABLE IV
IRON LOSS OF EACH PART OF THE MOTOR WHEN THE TURN ON AND TURN OFF ANGLE IS 30°–60°

Speed (r/min)	Stator pole (W)	Stator yoke (W)	Rotor pole (W)	Rotor yoke (W)	Total loss (W)
1000	14.81	53.66	9.06	9.85	87.38
1500	16.22	60.09	11.49	11.56	99.36
2000	18.43	63.91	12.11	12.32	106.77
2500	21.98	67.82	12.46	12.97	115.23

TABLE V
IRON LOSS OF EACH PART OF THE MOTOR WHEN THE TURN ON AND TURD OFF ANGLE IS 28°–60°

Speed (r/min)	Stator pole (W)	Stator yoke (W)	Rotor pole (W)	Rotor yoke (W)	Total loss (W)
1000	15.28	56.74	9.69	10.54	92.25
1500	16.85	63.99	12.30	12.40	105.54
2000	19.34	67.49	13.69	13.19	113.7
2500	22.93	71.62	13.46	13.08	121.09

TABLE VI
IRON LOSS OF EACH PART OF THE MOTOR WHEN THE TURN ON AND TURN OFF ANGLE IS 28°–62°

Speed (r/min)	Stator pole (W)	Stator yoke (W)	Rotor pole (W)	Rotor yoke (W)	Total loss (W)
1000	15.31	56.78	9.78	10.56	92.43
1500	19.28	66.60	12.20	12.34	110.42
2000	22.93	71.62	13.46	13.08	121.09
2500	25.42	73.52	14.16	13.43	126.53

Secondly, the peak values of the magnetic flux density waveforms of the stator and rotor parts are different.

Thirdly, the frequencies of the magnetic flux density waveforms of the stator and rotor are different, and the frequencies of the magnetic flux density waveforms of the rotor under different polarity distributions are also different. The superposition of these three causes leads to the ratio of iron loss produced by the stator part and the rotor part is about 4:1.

V. EXPERIMENTAL VERIFICATION

A. Iron Loss Measurement Methods

The iron loss cannot be measured directly, but can be obtained by two indirect measurement methods: calorimetric method [35] and elimination method [36]. The calorimetric method has strict requirements for the experimental environment, and the method requires a completely enclosed space which cannot exchange energy with the external space. The heat generated by the machine operating in an enclosed space leads to the temperature rise, and then the iron loss is determined by measuring the temperature rise. The elimination method is based on the energy conservation principle, and all the loss of the motor can be obtained by measuring the input and output parameters of the machine, and then the iron loss can be determined by eliminating the copper loss, mechanical loss and stray loss. The coupled circuit model of reluctance starter/generator is shown in Fig. 8. Compared with the harsh experimental environment required by the calorimetric method, the elimination method is easier to implement. Therefore, this paper uses the elimination method to measure the iron loss. The expression of the experimental measurement of iron loss is as follows:

$$P_{\mathrm{iron}} = (P_{\mathrm{in}} - P_{\mathrm{out}}) - (P_{\mathrm{cu}} + P_{\mathrm{tec}} + P_{\mathrm{stry}}) \tag{23}$$

where P_{in} , P_{out} , P_{cu} , P_{tec} , and P_{stry} are input power, output power, copper loss, mechanical loss, and stray loss, respectively.

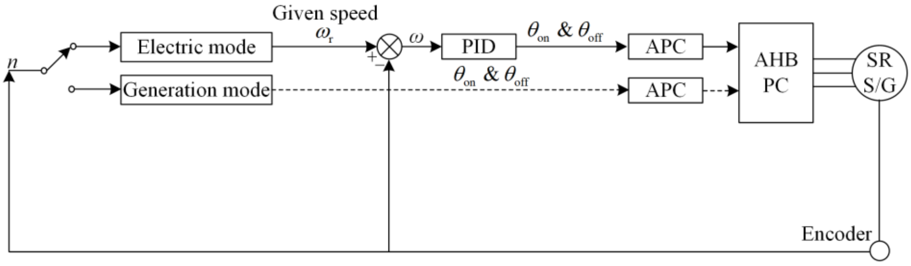

Fig. 8. Coupled circuit model of reluctance starter/generator.

The input power of SRG includes two parts: one is the mechanical power generated by the input torque of the prime motor, the other is the input power of the excitation power supply. The expressions of input power, output power, copper loss, mechanical loss and stray loss are as follows:

$$\begin{cases} P_{\mathrm{in}} = Tn/9.55 + U_{\mathrm{s}} I_{\mathrm{s}} \\ P_{\mathrm{out}} = U_{\mathrm{L}} I_{\mathrm{L}} \\ P_{\mathrm{cu}} = 3 I_{\mathrm{c}}^2 R_{\mathrm{c}} \\ P_{\mathrm{tec}} = T_0 n/9.55 \\ P_{\mathrm{stry}} = 0.06(P_{\mathrm{in}} - P_{\mathrm{out}}) \end{cases} \tag{24}$$

where T and n are the input torque and rotational speed, respectively; U_{s} and I_{s} are the excitation voltage RMS and excitation current RMS, respectively; U_{L} and I_{L} are the load voltage RMS and load current RMS, respectively; I_{c} and R_{c} are winding current and winding resistance, respectively; and T_0 is the no-load torque generated by the prime mover dragging an unexcited SRG.

Since the start-up process of SRS/G is very short, the iron loss generated during the start-up process is small and can be ignored. Therefore, the experiment in this paper mainly measures the iron loss generated during the power generation stage.

B. Experimental Platform

In order to verify the accuracy of the established iron loss simulation model, this paper builds an experimental platform for SRG iron loss measurement, and the experimental platform is shown in Fig. 9. In the power generation stage, SRG is driven by asynchronous motor to reach the specified speed. Iron loss measurement experiment adopts a three-phase asymmetric half-bridge power converter, an excitation voltage of 48 V and separate excitation mode.

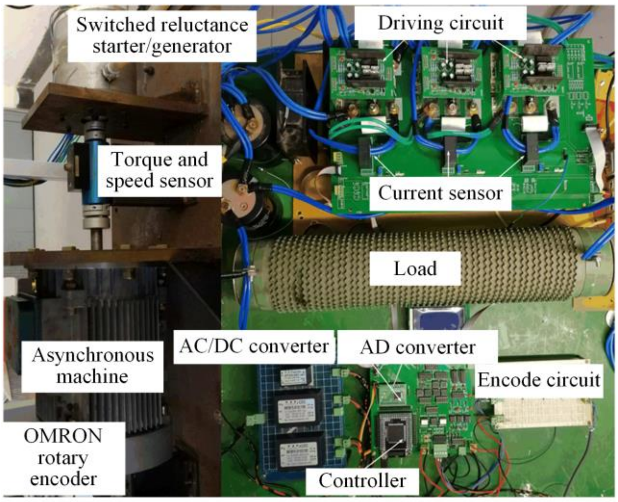

Fig. 9. Iron loss measurement experiment platform.

C. Iron Loss Measurement Results

In this paper, the iron loss at different rotational speeds and different turn-on and turn-off angles is measured, and the NNNSSS polarity distribution with smaller changing frequency of magnetic flux density waveform is adopted. When the conduction range is set to 30°–60°, the measured waveforms of winding phase current, load voltage and load current are shown in Fig. 10. Then the iron loss under various working conditions is measured according to the measurement method described in section V.A, and then the iron loss measured by the experiment is compared with the iron loss calculated by the simulation model in this paper. The comparison results are shown in Fig. 11. It can be seen from the waveforms comparison in Fig. 10 that there is a small error which is less than 10% between the experimental results and the calculation results of the iron loss, indicating the accuracy of the magnetic flux density waveform solution method combining the finite element method and the magnetic circuit analytic method, and indicating the accuracy of the Fourier fitting iron loss calculation model proposed in this paper.

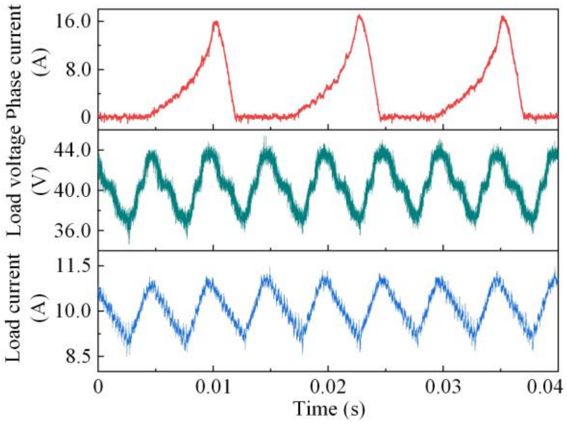

Fig. 10. Measurement waveforms of phase current, load voltage and load current.

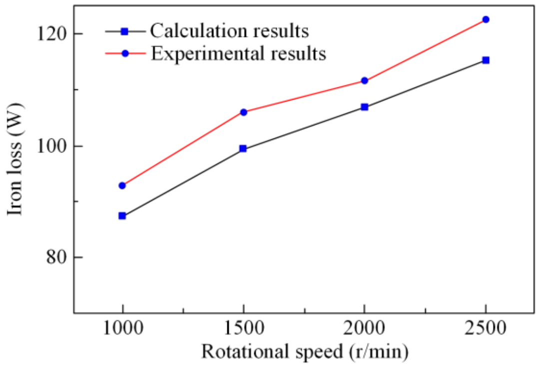

(a)

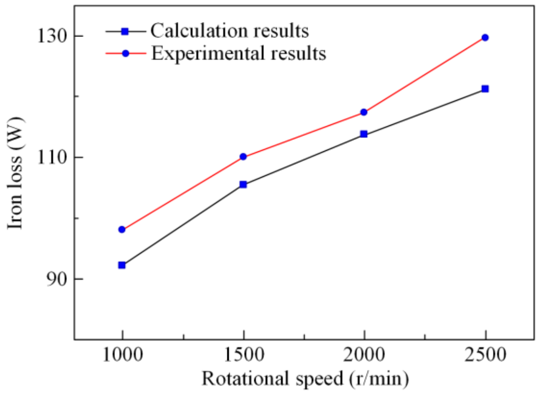

(b)

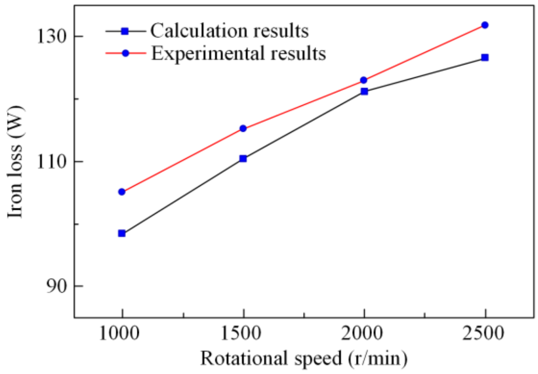

(c)

Fig. 11. Comparison of iron loss calculation results and experimental results under different turn-on and turn-off angles and speed conditions. (a) 30°–60°. (b) 28°–60°. (c) 28°–62°.

It can be found that under the same turn-on and turn-off angle, the iron loss value and iron loss comparison error of SRG at high rotational speed are relatively large. This is because the torque, current and voltage waveforms measured from experiment have large burrs at high speed, which affects the accuracy of measured data.

VI. CONCLUSION

In this paper, the solution of SRS/G iron loss is mainly divided into two parts: one is the solution of magnetic flux density waveforms, and another one is the establishment of iron loss model. Aiming at the characteristics of long time-consuming and poor universality of conventional FEM for solving magnetic flux density waveforms, this paper proposes a combination of the FEM and magnetic circuit analytic method. In view of the large error of iron loss coefficients fitted by polynomial fitting method under low frequency and low magnetic flux density, it adopts Fourier fitting method to fit the iron loss coefficients, and considers the influence of small hysteresis loop and skin effect to reduce the error under low frequency and low magnetic flux density. According to the solution characteristics of iron loss in different stages of SRS/G, this paper develops the both iron loss models for the time and frequency domains, where the time domain iron loss is suitable for the start-up stage, and the frequency domain iron loss is applicable to the power generation stage.

Since the start-up process of SRS/G is very short, the experiment in this paper mainly measures the iron loss generated during the power generation stage. The experimental results are compared with the simulation results of iron loss, and the error is less than 10 %, which verifies the accuracy of the iron loss calculation model. The accurate solution of SRS/G iron loss provides some reference and help for the development and improvement of power supply system of hybrid EVs, which contributes to the energy storage of hybrid EVs.

In future research, the algorithm can be improved from two aspects. First, intelligent algorithms can be used such as neural network and machine learning to obtain more accurate motor flux curves, further improving the accuracy of the algorithm. Secondly, in order to simplify the algorithm, the FEM is replaced by the experiment to obtain the magnetic flux of the motor. From the perspective of experimental fitting, a magnetic flux curve closer to the actual motor is obtained.

ACKNOWLEDGMENT

Not applicable.

AUTHORS' CONTRIBUTIONS

Hao Chen: full-text writing and innovative points proposing. Xing Wang: guidance on article structure. Yongqiang Liu: software and simulations. Vuong Dang Quoc: complete revision. Wenju Yan: English improvement and construction of the paper framework. Muhammad Asghar Saqib: experimental guidance. Antonino Musolino: format adjustment. Guanjun Wang: experimental assistance. Qi Yong: English improvement. Ali Asghar Memon: improvement of experimental methods. Alexandros G. Paspatis: simulation guidance. All authors contributed to the final version of the manuscript.

FUNDING

This work is supported in part by the Shenzhen Collaborative Innovation Special Plan International Cooperation Research Project (No. GJHZ20220913144400001) and the General Research Project of Shenzhen Science and Technology Plan (No. JCYJ20220818100000001).

AVAILABILITY OF DATA AND MATERIALS

Not applicable.

DECLARATIONS

Competing interests: The authors declare that they have no known competing financial interests or personal relationships that could have appeared to influence the work reported in this article.

AUTHORS' INFORMATION

Hao Chen received B.S. and Ph.D. degrees in electrical engineering from the Department of Automatic Control, Nanjing University of Aeronautics and Astronautics, Nanjing, China, in 1991 and 1996, respectively. In 1998, he became an associate professor with the School of Information and Electrical Engineering, China University of Mining and Technology, Xuzhou, China, where he has been a Professor since 2001. From 2002 to 2003, he was a visiting professor at Kyungsung University, Busan, Korea. Since 2008, he has also been an adjunct professor at the University of Western Australia, Perth, Australia. He is the author of one book and has also authored more than 200 papers. He is the holder of 15 US Patents, 23 Australian Patents, 1 Danish Patent, 7 Canadian Patents, 3 South African Patents, 10 Russian Patents, 76 Chinese Invention Patents and 6 Chinese Utility Model Patents. His current research interests include motor control, linear launcher, EVs, electric traction, servo drives, and wind power generator control.

Xing Wang received her B.S. degree from China University of Mining and Technology in computer science and technology and received her master's degree from China University of Mining and Technology in management engineering. Now she is the associate professor of China University of Mining and Technology, Xuzhou, China.

Yongqiang Liu received the B.S. degree from the School of Electrical Engineering, Nantong University, Nantong, China, in 2019. And He received his M.S. degree in electrical engineering with the China University of Mining and Technology, Xuzhou, China, in 2022. His research interests include integrated drive systems for EVs and double-stator switched reluctance motors.

Vuong Dang Quoc received his Ph.D. degree in electrical engineering in July 2013 at the Faculty of Applied Sciences at the University of Liège in Belgium. After that he came back to the Hanoi University of Science and Technology in September 2013, where he is currently working as a deputy director of Training Center of Electrical and Electrical Engineering, School of Electrical Engineering (SEEE), Hanoi University of Science and Technology (HUST). He became an associate professor in 2020. Assoc. Prof. Dang Quoc Vuong's research domain encompasses modeling of electromagnetic systems, electrical machines, optimization method, numerical methods and subproblem methods.

Wenju Yan received the B.S. degree in electrical engineering and automation and the Ph.D. degree in electrical engineering from the China University of Mining and Technology, Xuzhou, China, in 2013 and 2018, respectively. From 2019 to 2021, he was a Post-Doctoral Research Fellow with the China University of Mining and Technology, where he has been an Associate Professor since 2021. His current research interests include EVs, electric traction, iron loss analysis, and special motor design.

Muhammad Asghar Saqib graduated in electrical (power) engineering from the Department of Electrical Engineering, University of Engineering and Technology, Lahore, Pakistan, in 1991. He received the master's and Ph.D. degrees in electrical (power) engineering from The University of Sydney, Sydney, NSW, Australia, in 1996 and 1999, respectively. He was an AusAID Scholar. He then joined the Faculty of Electronics Engineering, Ghulam Ishaq Khan Institute of Engineering (GIK Institute), Topi, Pakistan, as an assistant professor and became an associate professor and the dean of the faculty in 2005. In December 2005, he joined the Department of Electrical Engineering, University of Engineering and Technology, as an associate professor and became a professor in November 2017, where he is also the director of the High Voltage Engineering Laboratory. His research interests are in the areas of power electronics and electrical drives, renewable energy, and power systems.

Antonino Musolino received the Ph.D. degree in electrical engineering from the University of Pisa, Pisa, Italy, in 1994. He is currently a full professor of electrical machines with the University of Pisa. He has coauthored more than 130 papers published in international journals/conferences. He holds three international patents in the field of magnetorheo-logical devices. His current research activities are focused on linear electromagnetic devices, motor drives for electric traction, and the development of analytical and numerical methods in electromagnetics.

Guanjun Wang now is working at Wuxi Inspection and Testing Certification Research Institute, Wuxi, Jiangsu, China.

Yong Qi received his B.S. degree and Ph.D. degree from Nanjing University of Science and Technology. Now he is the professor of Nanjing University of Science and Technology.

Ali Asghar Memon is the professor of Mehran Engineering University in Pakistan.

Alexandros G. Passatis received his Ph.D. degree in automatic control and systems engineering from the University of Sheffield in the UK in 2020. Since 2023, he has served as an assistant professor at Manchester City University, UK. His main directions include power inverter control, inverter drive stability, microgrids, and laboratory validation methods.

REFERENCES

[1] W. Liu, Y. Bian, and S. Wu *et al.*, "Overview and prospect of carbon emission accounting in electric power systems," *Power System Protection and Control*, vol. 52, no. 4, pp. 176-187, Feb. 2024. (in Chinese)

[2] S. Qi, Z. Yao, and Y. Liao *et al.*, "Online probabilistic assessment of static voltage stability margin for power systems with a high proportion of renewable energy," *Power System Protection and Control*, vol. 51, no. 5, pp. 47-57, Mar. 2023. (in Chinese)

[3] J. Yun, S. Zhang, and G. Zhang *et al.*, "Optimal operation of an integrated energy system considering integrated demand response and a "dual carbon" mechanism," *Power System Protection and Control*, vol. 50, no. 16, pp. 11-19, Nov. 2022. (in Chinese)

[4] O. Olujobi, "The legal sustainability of energy substitution in Nigeria's electric power sector: renewable energy as alternative," *Protection and Control of Modern Power Systems*, vol. 5, no. 4, pp. 1-12, Oct. 2020.

[5] K. Xie, H. Hui, and Y. Ding, "Review of modeling and control strategy of thermostatically controlled loads for virtual energy storage system," *Protection and Control of Modern Power Systems*, vol. 4, no. 4, pp. 1-13, Oct. 2019.

[6] H. Shen, G. Chen, and Y. Zhao *et al.*, "Orderly charging optimization strategy of an electric vehicle based on double objective hierarchical optimization and TOPSIS ranking," *Power System Protection and Control*, vol. 49, no. 11, pp. 115-123, Jun. 2021. (in Chinese)

[7] S. Koohi-Fayegh and M. Rosen., "A review of energy storage types, applications and recent developments," *Journal of Energy Storage*, vol. 27, no. 1, pp. 16-27, Jan. 2020.

[8] Y. Mi, B. Chen, and P. Cai *et al.*, "Frequency control of a wind-diesel system based on hybrid energy storage," *Protection and Control of Modern Power Systems*, vol. 7, no. 3, pp. 1-13, Jul. 2022.

[9] S. Wang, Q. Zhan, and Z. Ma, *et al.*, "Implementation of a 50-kW four-phase switched reluctance motor drive system for hybrid EV," *IEEE Transactions on Magnetics*, vol. 41, no. 1, pp. 501-504, Jan. 2005.

[10] K. Chau and C. Chan, "Emerging energy efficient technologies for hybrid EVs," Proceedings of the IEEE, vol. 95, no. 1, pp. 821-835, Jan. 2007.

[11] K. T. Chau, C. C. Chan, and C. Liu, "Overview of permanent-magnet brushless drives for electric and hybrid electric vehicles," *IEEE Transactions on Industrial Electronics*, vol. 55, no. 6, pp. 2246-2257, Jun. 2008.

[12] J. Faiz and K. Moayed-Zadeh, "Design of switched reluctance machine for starter/generator of hybrid EV," *Electric Power Systems Research*, vol. 75, no. 1, pp. 153-160, Jan. 2005.

[13] E. Zhao, S. Song, and Y. Li *et al.*, "Design and initial testing of an integrated switched reluctance starter/generator system for unmanned aerial vehicle," *CES Transactions on Electrical Machines and Systems*, vol. 2, no. 1, pp. 377-383, Jan. 2019.

[14] M. Wardach, R. Palka, and P. Paplicki *et al.*, "*Modern Hybrid Excited Electric Machines*," *Energies*, vol. 13, no. 22, Nov. 2020.

[15] W. Yan, H. Chen, and L. Chen *et al.*, "Iron loss analysis on switched reluctance motor under different control modes," *IET Electric Power Applications*, vol. 11, no. 1, pp. 1575-1584, Jan. 2017.

[16] J. Reinert, A. Brockmeyer, and R. De Doncker, "Calculation of losses in ferro and ferrimagnetic materials based on the modified Steinmetz equation," *IEEE Transactions on Industry Applications*, vol. 37, no. 4, pp. 1055-1061, Jul.-Aug. 2001.

[17] Y. Hayashi and T. Miller, "A new approach to calculating core losses in the SRM," *IEEE Transactions on Industry Applications*, vol. 31, no. 5, pp. 1039-1046, Sept.-Oct. 1995.

[18] M. Hassanin, M. Alrifai, and D. Torrey, "Experimentally verified flux density models for the switched-reluctance machine," *IEEE Transactions on Magnetics*, vol. 37, no. 5, pp. 3818-3824, Sept. 2001.

[19] Q. Yu, B. Bilgin, and A. Emadi, "Loss and efficiency analysis of switched reluctance machines using a new calculation method," *IEEE Transactions on Industrial Electronics*, vol. 62, no. 5, pp. 3072-3080, May 2015.

[20] Y. Lin, E. Zhou, and J. Huang *et al.*, "Finite element analysis and iron loss calculation of switched reluctance motor magnetic field," *Transactions of China Electrotechnical Society*, vol. 11, no. 1, pp. 24-29, Jan. 1996.

[21] B. Ganji, J. Faiz, and K. Kasper *et al.*, "Core loss model based on finite-element method for switched reluctance motors," *IET Electric Power Applications*, vol. 4, no. 1, pp. 569-577, Jan. 2010.

[22] L. Chen, H. Chen, and W. Yan, "A fast iron loss calculation model for switched reluctance motors," *IET Electric Power Applications*, vol. 11, no. 1, pp. 478-486, Jan. 2017.

[23] N. Sadowski and M. Lajoie-Mazenc. "Evaluation and analysis of iron losses in electrical machines using the rain-flow method," *IEEE Transactions on Magnetics*, vol. 36, no. 4, pp. 1923-1926, Jul. 2000.

[24] W. Yan, H. Chen, and L. Chen, "Analysis on iron loss of switched reluctance motor under PWM mode," *COMPEL* - The International Journal for Computation and Mathematics in Electrical and Electronic Engineering, vol. 37, no. 1, pp. 448-464, Jan. 2017.

[25] J. Powell, W. Jewel, and D. Calverley, "Iron loss in a modular rotor switched reluctance machine for the "more-electric" aero-engin," *IEEE Transactions on Magnetics*, vol. 41, no. 10, pp. 3934-3936, Oct. 2005.

[26] N. Arbab, W. Wang, and C. Lin *et al.*, "Thermal modeling and analysis of a double-stator switched reluctance motor," *IEEE Transactions on Energy Conversion*, vol. 30, no. 3, pp. 1209-1217, Sept. 2015.

[27] Z. Cheng, N. Takahashi, and B. Forghani *et al.*, "3-D finite element modeling and validation of power frequency multishielding effect," *IEEE Transactions on Magnetics*, vol. 48, no. 2, pp. 243-246, Feb. 2012.